Materials Chemistry and Physics 136 (2012) 528–537

Contents lists available at SciVerse ScienceDirect

Materials Chemistry and Physics

journal homepage: www.elsevier.com/locate/matchemphys

One pot synthesis of silver nanoparticles supported on TiO_2 using hybrid polymers as template and its efficient catalysis for the reduction of 4-nitrophenol

Mohamed Mokhtar Mohamed [a,b,*], Merfat S. Al-Sharif [c]

[a] Benha University, Faculty of Science, Chemistry Department, Benha, Egypt
[b] Umm Al-Qura University, Faculty of Applied Science, Chemistry Department, Makkah, Saudi Arabia
[c] Al-Taief University, Faculty of Science, Chemistry Department, Al-Taief, Saudi Arabia

HIGHLIGHTS

- One pot facile hydrothermal synthesis of Ag/TiO_2 using hybrid polymers as template.
- The prepared nanomaterials revealed high activities on the reduction of 4-nitrophenol.
- Catalysts characterized by BET, FTIR, TEM, XRD and UV–vis spectroscopy.
- Morphologies and surface texturing of the materials played main role in the reduction.

GRAPHICAL ABSTRACT

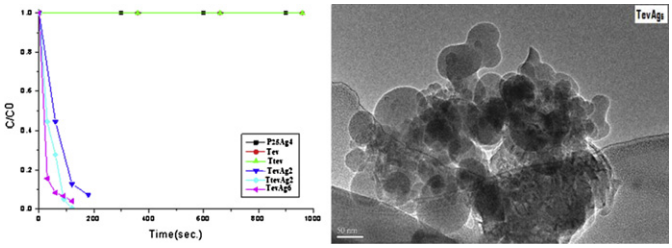

ARTICLE INFO

Article history:
Received 10 May 2012
Received in revised form
9 July 2012
Accepted 21 July 2012

Keywords:
4-Nitrophenol reduction
Composite materials
Electron microscopy
Surface properties

ABSTRACT

Hybrid TiO_2 nanostructures with engineered morphologies (flakes, spheres and buds) supporting Ag nanocrystals were produced by a simple synthetic approach based on cooperative sol–gel chemistry of either titanium iso-propoxide or n-butoxide and self-assembly of polyvinyl alcohol with polyethylene glycol. The as-synthesized catalysts were characterized using XRD, TEM, DRUV–Vis, N_2 sorptiometry and FTIR spectroscopy and their performances toward 4-nitrophenol (4-NP) reduction were also investigated. Among the structures investigated, the catalyst derived from n-butoxide (Ttev) exhibited the best catalytic performance in the reduction of 4-NP to 4-aminophenol (4-AP) in 2 min with 100% conversion when loaded with 2% Ag ions ($TtevAg_2$). In concordance, the $TevAg_6$ catalyst; derived from isopropoxide, of bud shape and particle sizes of 20 nm showed a comparable activity to that of $TtevAg_2$ and exhibited a rate constant of 6.9×10^{-3} s^{-1} resembling that of 7.2×10^{-3} s^{-1} for $TtevAg_2$ exceeding that of $TevAg_2$. Enhancing the activity of $TevAg_6$ and $TtevAg_2$ compared to $TevAg_2$ was rationalized in terms of the surface content of Ag^o nanoparticles of medium sizes (15–20 nm) inside mesoporous network of TiO_2 of tailored morphology (proportional amounts of buds and spheres structures) as well as pore volume values. No deactivation for the former catalysts was observed after repeated recycling.

1. Introduction

Aromatic amines are important organic pollutants and are intermediates or side products of many industrial products such as dyes, pharmaceuticals, agro-chemicals, cosmetics, photographic chemicals, chelating agents, and so on [1–4]. The hydrogenation of a range of aliphatic [5] and aromatic [6] nitro-compounds in both gas [3,7] and liquid [8,9] phase process, is difficult to achieve in the presence of other reactive substituents (e.g. –Cl, $-CH_3$ and/or

* Corresponding author. Umm Al-Qura University, Faculty of Applied Science, Chemistry Department, Makkah, Saudi Arabia. Tel.: +966 500969808; fax: + 966 5561107.
E-mail address: mohmok2000@yahoo.com (M.M. Mohamed).

0254-0584/$ – see front matter © 2012 Elsevier B.V. All rights reserved.
http://dx.doi.org/10.1016/j.matchemphys.2012.07.021

–OH). The conventional synthesis route for amino-derivates, using stoichiometric amounts of Fe in acid media (Bechamp process) is no longer being continued due to the formation of Fe–FeO sludge waste that produces pollution problems as well as low selectivites/product yields [10]. Therefore, a great number of studies for reduction of *p*-nitrophenol to *p*-aminophenol have been performed over the past few decades [6,11,12]. The catalytic (liquid phase) alternative using standard transition metals (e.g. Ni [13], Pd [14], and/or Pt [15]) also exhibits limitations in terms of unfavorable toxic secondary reaction products, i.e. azo- [16] and/or azoxy-derivates [17]. Some of these methods are employing reduction with $NaBH_4$ in the presence of palladium nanoparticles [18], silver nanoparticles [19], gold nanoparticles [20], and reduction with H_2 in the presence of Ni–B alloy catalysts [21], reduction with hydrazine hydrate in the presence of Ni particles [22], and reduction with iron powder or stannous chloride under ultrasonic irradiation [23]. In general, supported Ag [14–26] exhibits lower hydrogenation activities relative to typical transition metal catalysts [13–15,22]. There is evidence [27–29] of a structure sensitive response in the case of Au where increased efficiency is attributed to smaller particles ($\leq$10 nm). Theoretical calculations have demonstrated a high energy barrier for H_2 dissociation on group IB metals [30] and, in the case of Au catalysts, H_2 activation has been associated with step, edge and corner sites on small Au particles [31].

A variety of approaches have been attempted to prepare Ag/TiO_2 supported nanoparticle catalysts, for instance, photodeposition, chemical deposition and conventional impregnation method [32]. In the earlier work, most of the Ag/TiO_2 nanocomposites were composed of randomly mixed TiO_2 and Ag nanoparticles [33,34]. However, TiO_2 nanoparticles tend to agglomerate leading to decrease in surface area and phase separation during repeated utilization. Moreover, if the Ag nanoparticles cannot be well dispersed on the surface of TiO_2, the density of active sites on the Ag/TiO_2 surface will be incompetent. In addition, silver doped TiO_2 (Ag/TiO_2) nanocomposite structures have attracted much attention not only because TiO_2 is a promising material with desirable electronic and optical properties, but also because Ag displays some unique activities in chemical and biological sensing compared with the other noble metals mentioned above [35,36]. To date, it has been shown in many reports that either impregnation or photodeposition of noble metals with TiO_2 could effectively cause dramatic problems for instance low dispersion, low stability as well as particles size enlargements [37–39]. Other methods involving sol–gel, 'wet' chemical and ceramic methods, where drying, heating or annealing at high temperatures are important steps in the preparation process [40–42], are too complicated in the sense of revealing low Ag dispersion. On the other hand, it has been acknowledged that the polyol process is a convenient, versatile and low-cost method for the synthesis of metal nanostructures. Based on this technique, a number of metal nanostructures, such as gold nano-octahedra [43], gold nanoplates [44] Ag nanowires [45] and Ag nanopowder [46], have been successfully synthesized in ethylene glycol (EG) solution.

In order to modify the TiO_2 by Ag nanoparticles, we demonstrated that one pot reaction using a combined template composed of polyvinyl alcohol and polyethylene glycol can be utilized for the in-situ Ag/titania nanoparticles preparation. The most relevant synthetic characteristic is the use of a hybrid polymer as template to produce mesoporosity in the material with tailorable morphology. The synthesized materials have been thoroughly characterized by XRD, TEM, N_2 sorptiometry, FTIR and UV–Visible diffuse reflectance spectroscopy. The reduction of silver ions in Ag/TiO_2 is carried out during the reduction process of 4-nitrophenol; to its corresponding aminophenol, via employing $NaBH_4$. The progress of the reduction reactions was followed by UV–vis spectrophotometer. The effects of catalyst and reduction agent amounts on the reduction of 4-nitrophenol were investigated at room temperature.

2. Experimental

2.1. Assembly of Ag nanoparticles in TiO_2

TiO_2 nanoparticles were fabricated by self assembly method according to the following procedure. Briefly, Polyethylene glycol ($HO(CH_2CH_2O)_nH$-0.01 M) and polyvinyl-alcohol ($CH_2–CH(OH)_n–$0.01 M) dissolved in a least amount of water (15 ml) in a weight ratio of 7:3 were mixed thoroughly. Titanium iso-propoxide ($Ti(OCH(CH_3)_2)_4$-29.3 ml) was added into the above mixture via a drop wise manner with vigorous stirring for half an hour at room temperature. The resulting reaction mixture was transformed into an autoclave lined with Teflon followed by hydrothermal treatment at 393 K for 48 h. After hydrothermal treatment, the product was recovered by centrifugation and then washed 3 times with deionized water. The solid was then dried overnight at 333 K and further calcined in air at 673 K for 6 h to remove the copolymer template. This sample was denoted as Tev, where the letter e expresses polyethylene glycol and v expresses polyvinyl-alcohol. Different weight % were prepared in Ag/TiO_2 ratios at which $AgNO_3$ insertion took place at a ratio of either 2% or 6% in a solution form before titanium iso-propoxide admission took place to prepare samples denoted as $TevAg_2$ and $TevAg_6$. In the same way titanium tetra-butoxide ($Ti(O(CH_2)_3CH_3)_4$-30 ml) was used instead of titanium isopropoxide to synthesize samples denoted as Ttev; where t represents titanium tetra-butoxide, and $TtevAg_2$ that signifies the sample with silver insertion ratio of 2%. Scheme 1 shows the generation of self-assembled hybrid arrays of Ag/TiO_2 using polyethylene glycol and polyvinyl alcohol templates. TiO_2 P25 (70% anatase:30% rutile) with a surface area of 49 $m^2\ g^{-1}$ and primary crystal size 30 nm that purchased from Degussa was impregnated with $AgNO_3$ at a ratio of 4% by dispersing TiO_2 powder in 30 ml ethanol followed by addition of $AgNO_3$ solution to give a catalyst denoted as $P_{25}Ag_4$, for comparison purposes. Different patches were synthesized for the Ag/TiO_2 catalysts following up the same procedure and as a result a good reproducibility has been attained.

2.2. Physicochemical characterization of materials

2.2.1. X-ray diffraction analysis

X-ray diffraction analysis was performed on X-Ray Diffraction (XRD) spectrometer Model XRD 8030 from Jeol co., Japan. Maximum power is 3 kw and the unit is equipped with rotating stage and thin layer accessories. The patterns were run with Co-filtered CoKα radiation (λ = 1.79 Å) energized at 45 kV, and 10 mA. The counter is scintillation with dead 10^{-6} s. The samples were measured at room temperature in the range of $2\theta = 20–80°$. The XRD phases present in the samples were identified with the help of ASTM Powder Data Files.

2.2.2. Fourier transform infrared spectra (FT-IR)

The infrared spectra of the samples were recorded in the range of 400–4000 cm^{-1}. The method includes mixing few mgs of a fine powder of the sample with KBr powder in agate mortar. The mixture was then pressed by means of hydraulic press. The transmission was automatically registered against wavenumber (cm^{-1}) using a Perkin–Elmer instrument (Spectrum GX), made in USA.

2.2.3. Transmission electron microscope (TEM)

The observation of the particle shape and the measurement of the particle size distribution of the precipitate was performed using

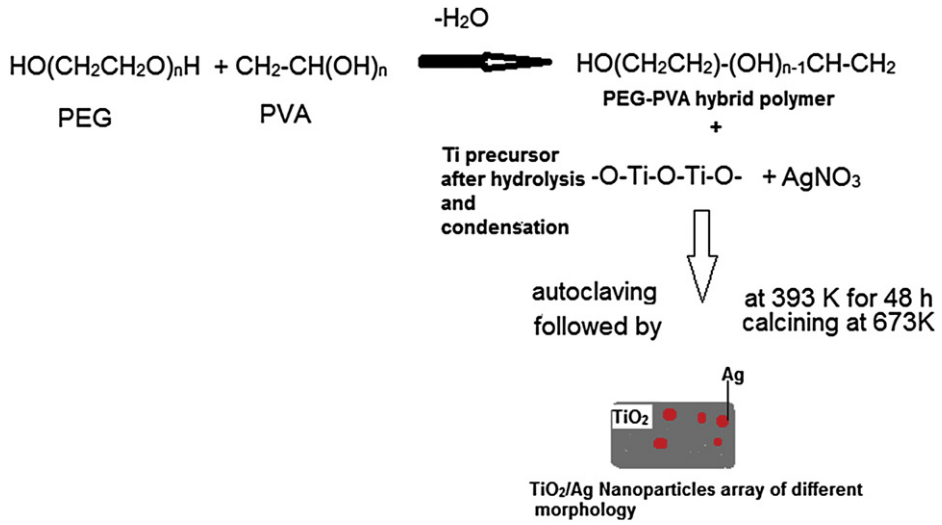

Scheme 1. Diagram of the generation of self-assembled hybrid arrays of Ag/TiO_2 using polyethylene glycol and polyvinyl alcohol templates.

a JEM-2100F transmission Electron Microscope (JEOL) using conductive carbon paint. The strength is 200 kV with 0.23 nm sensitivity.

2.2.4. Nitrogen adsorption measurements

Nitrogen adsorption measurements were performed at liquid nitrogen temperature with a Micromeritics ASAP 2020 surface area and porosity analyzer. Prior to the measurements, the samples were degassed for half an hour at 363 K followed by 3 h at 473 K. Surface area was calculated using the BET (Brunauer–Emmett–Teller) interpretation of the nitrogen adsorption isotherm. The pretreatment conditions must remain sufficiently mild to avoid any modification of the textural characteristics of the sample but severe enough to obtain a good surface clean-up.

2.2.5. Ultraviolet–visible diffuse reflectance spectroscopy

Diffuse Reflectance Ultraviolet–visible spectroscopy (UV–vis DRS) of powder catalyst samples was carried out at room temperature using a Perkin–Elmer Lamda-35 spectrophotometer in the range of 200–800 nm.

2.2.6. Activity measurements by catalytic reduction of 4-NP

To investigate the catalytic reduction of 1.8×10^{-4} mol L^{-1} 4-NP, a 300 ml glass reactor was charged with definite amounts of catalysts at 298 K and mixed with [4-NP] till the volume of the water reaches 100 ml with deionized water. Then 5 ml of $NaBH_4$ at 2.0×10^{-1} mol L^{-1} concentration was rapidly injected under constant stirring. The yellow color of solution gradually vanished, indicating the reduction of 4-NP. During the hydrogenation, catalysts were suspended in solution by violent stirring. The temperature and pressure in the reactor were maintained at room temperature and at atmospheric pressure, respectively. Samples were directly withdrawn from the reaction medium at certain time intervals followed by measuring UV–vis; using a Hitachi U-3000 spectrophotometer, spectra of these solutions to monitor the decrease in intensity of the absorption peak at 400 nm for 4-NP. The rate constant of the reaction was determined by measuring the change in intensity of these peaks with time. The progress of the reactions was followed at room temperatures (25 °C), and the activation parameters for the reduction reactions of 4-NP to their corresponding amine forms, 4-aminephenol, were calculated. At the end of the reaction, the catalysts were separated from the suspension containing Ag/TiO_2 nanocatalysts and the residual amount of Ag species were monitored using ICP (Horiba) spectrometer to stand on their dispersity in TiO_2 catalysts. The product 4-aminophenol was also identified by capillary column gas chromatography (Varian 3900).

3. Results and discussion

3.1. Phase composition and morphologies of the samples

The results of XRD analysis of synthesized titania nanopowders derived from polyethylene glycol and polyvinyl alcohol as hybrid polymers together with those incorporated with Ag ions (Table 1 and Fig. 1), confirm the findings of anatase (JCPDS 21-1272) as a major phase and rutile (JCPDS 21-1276) as a minor one. A quantitative analysis of the phase composition of titania is performed by examining the XRD patterns by calculating the integrated intensities of anatase (1 0 1) and rutile (1 1 0) peaks [47]. It can be seen that varying the titanium precursor from isopropoxide into n-butoxide did not affect much the ratio of anatase to rutile apart from the Ttev sample that stimulates the formation of brookite phase at 30.8° at a ratio of 10% beside the anatase one. However, incorporation of Ag at a loading of 2% affects the ratio of anatase to 76% in $TtevAg_2$ and 90% in $TevAg_2$. Interestingly, increasing the ratio of Ag into 6% preserve the % crystallinity of anatase in $TevAg_6$ to 93% compared with 97% in Tev sample, proposing that major part of Ag ions were

Table 1
Crystallinity, particles size and lattice spacing of TiO_2 and Ag/TiO_2 synthesized using hybrid polymer template via self-assembly method.

Sample	Crystalinity[a]			Particle size(nm)[b]	Lattice parameter (Å)		Lattice volume (Å^3)
	Anatase	Rutile	Brookite		A	B C	
Tev	97	3.0	–	10.0	3.785	9.514	136.30
$TevAg_2$	90	–	–	5.0	3.785	9.514	136.30
Ttev	90	–	10	10.0	3.785	9.514	136.30
$TtevAg_2$	76	24	–	15.0	3.785	9.514	136.30
$TevAg_6$	93	–	–	10.0	3.785	9.514	136.30

[a] The crystallinity of the samples were measured from the integrated intensities of anatase (1 0 1), rutile (1 1 0) and brookite (121) peaks using respectively the following formulas: $W_A = k_A A_A/(k_A A_A + A_R)$, $W_R = A_R/(k_A A_A + A_R)$ and $W_B = A_B/(k_A A_A + A_B)$.

[b] Crystallite sizes are determined by the broadening of the TiO_2 (101) facet for anatase diffraction peak using the Scherrer formula.

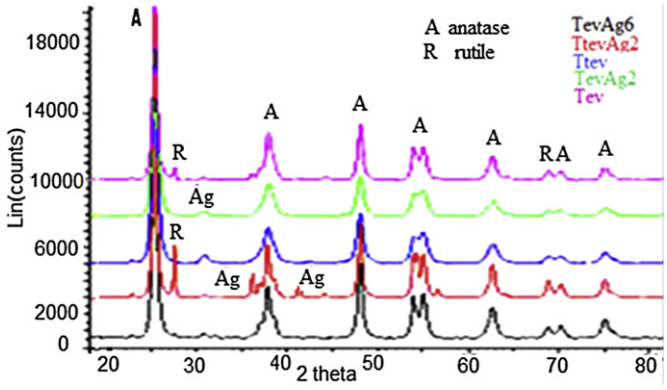

Fig. 1. XRD patterns of Tev, $TevAg_2$, Ttev, $TtevAg_2$ and $TevAg_6$.

not in good interaction with the titania substrate. Accordingly, very small lines in the 2θ range from 30 to 35° were clearly depicted corresponding to Ag_2O species besides a hardly defined line; due to interference with the anatase line at $2\theta = 38.5°$, due to Ag^o. The Particles size determined using Scherrer equation were comparable for all samples to be around 10.0 nm except $TevAg_2$ and $TtevAg_2$ those showed sizes of 5 and 15 nm, respectively. This could give a hint on the effect of the titania precursor on its crystallites size and consequently on the morphology of incorporated ions, as will be seen later.

Incorporating Ag in Ttev at a loading of 2% ($TtevAg_2$) not only decreases the anatase phase content into 76% and but also enhances the rutile phase content into 24% beside vanishing those of brookite (10%); in Ttev, along with depicting small peaks due to Ag_2O at $2\theta = 36, 41.9, 56°$ and Ag^o at 38.1° (111) and 44° (200). This suggests the monolayer accumulation of either Ag_2O and/or Ag^o over TiO_2 support; derived from Ti (IV) n-butoxide, highlighting the effect of titania precursor on exposing silver oxides/metal nanoparticles rather than their dispersion as in $TevAg_2$. Accordingly, the diminished interaction between Ag ions and titania in $TtevAg_2$ was responsible for exposing Ag_2O moieties and increasing crystallites size of titania particles into 15 nm.

Fig. 2a shows the TEM image of Tev that exhibits mean particle sizes in the 10–16 nm range and acquires mainly a nano flakes like morphology. The particle size distribution was narrow and slightly-aggregated. Due to the distinctive difference in electron densities, Ag deposited on TiO_2 is readily identified as black spots where the outer TiO_2 appears lighter. In concordance, Fig. 2b shows the TEM image of $TevAg_2$ where the shape is changed into spherical-like structure with an average crystallite size in the 2.0–10 nm range for titania wherein Ag is highly dispersed providing average particles size of 2 nm, assigning their absence in the XRD pattern for the instrument detection limit (≥4 nm). Such small NPs (2 nm) play an important role for the photocatalytic performance. Meanwhile, the small NPs can serve as an electron conductor, which facilitates photoelectron transfer and further reduce the probability of charge recombination. As can be seen in the TEM image (Fig. 2b), the lattice fringes exhibit the typical distance of 3.54 Å that agrees with the (101) lattice spacing of anatase TiO_2 [48]. It is important to note that the incorporation of Ag nanoparticles into the TiO_2 framework does not destroy the latter's mesostructure.

Fig. 2c shows the TEM image of the $TevAg_6$ sample that showed varying morphology compared with that of $TevAg_2$. It shows bud shape beside spherical-like ones as a result of increasing the Ag content into 6%. The average particles size of titania substrate was in the 30–100 nm range. From the high resolution TEM (HR-TEM) image, one can see that the AgNPs are mostly single crystalline with average crystallites of 20 nm. The variation of crystallites size of this

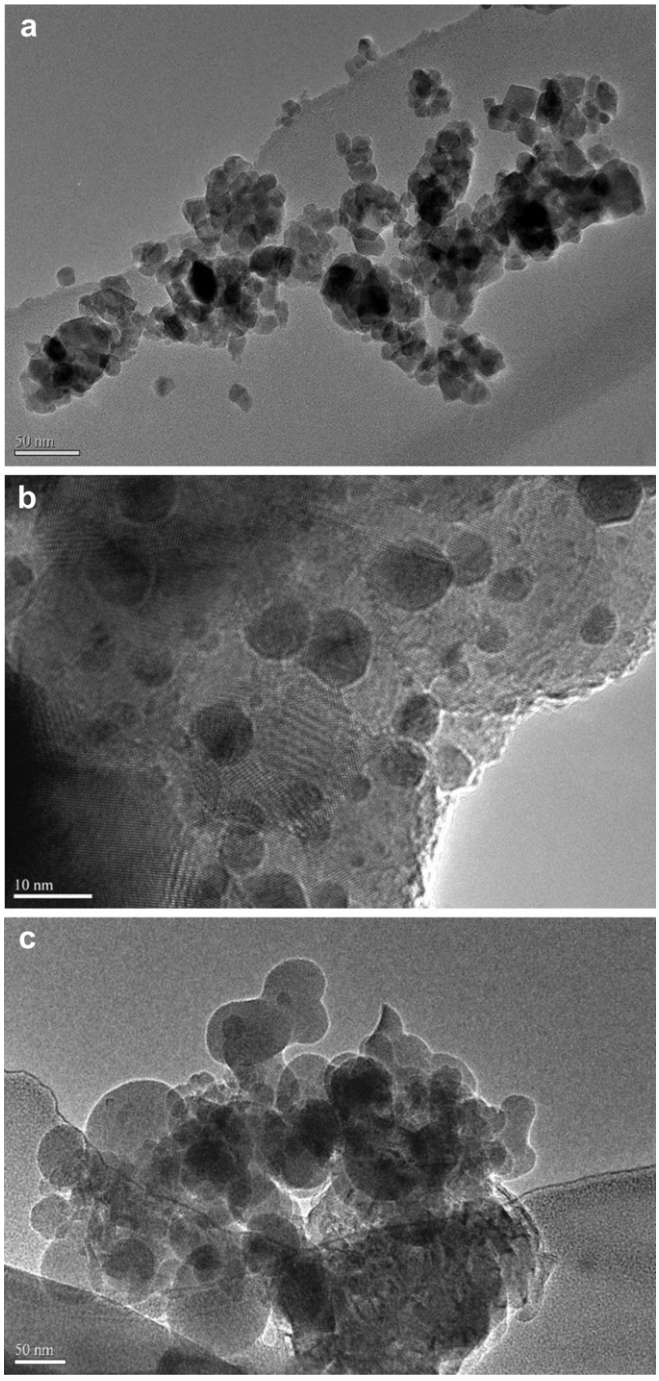

Fig. 2. (a) TEM image of Tev. (b) TEM image of $TevAg_2$. (c) TEM image of $TevAg_6$.

particular sample when measured by TEM and XRD band width could be due the presence of very small crystallite sizes that led to extreme peak broadening in XRD hindering it to distinguish the nanocrystalline phase of TiO_2 anatase.

3.2. Surface texturing properties

Fig. 3a gives N_2 adsorption–desorption isotherm of the Tev sample that belongs to a mixed type, in the IUPAC classification, composed of type II at high relative pressures (P/P^o) and type IV at intermediate relative pressures. The pore-size distribution obtained for Tev (Fig. 3b) from N_2 adsorption indicates that it is

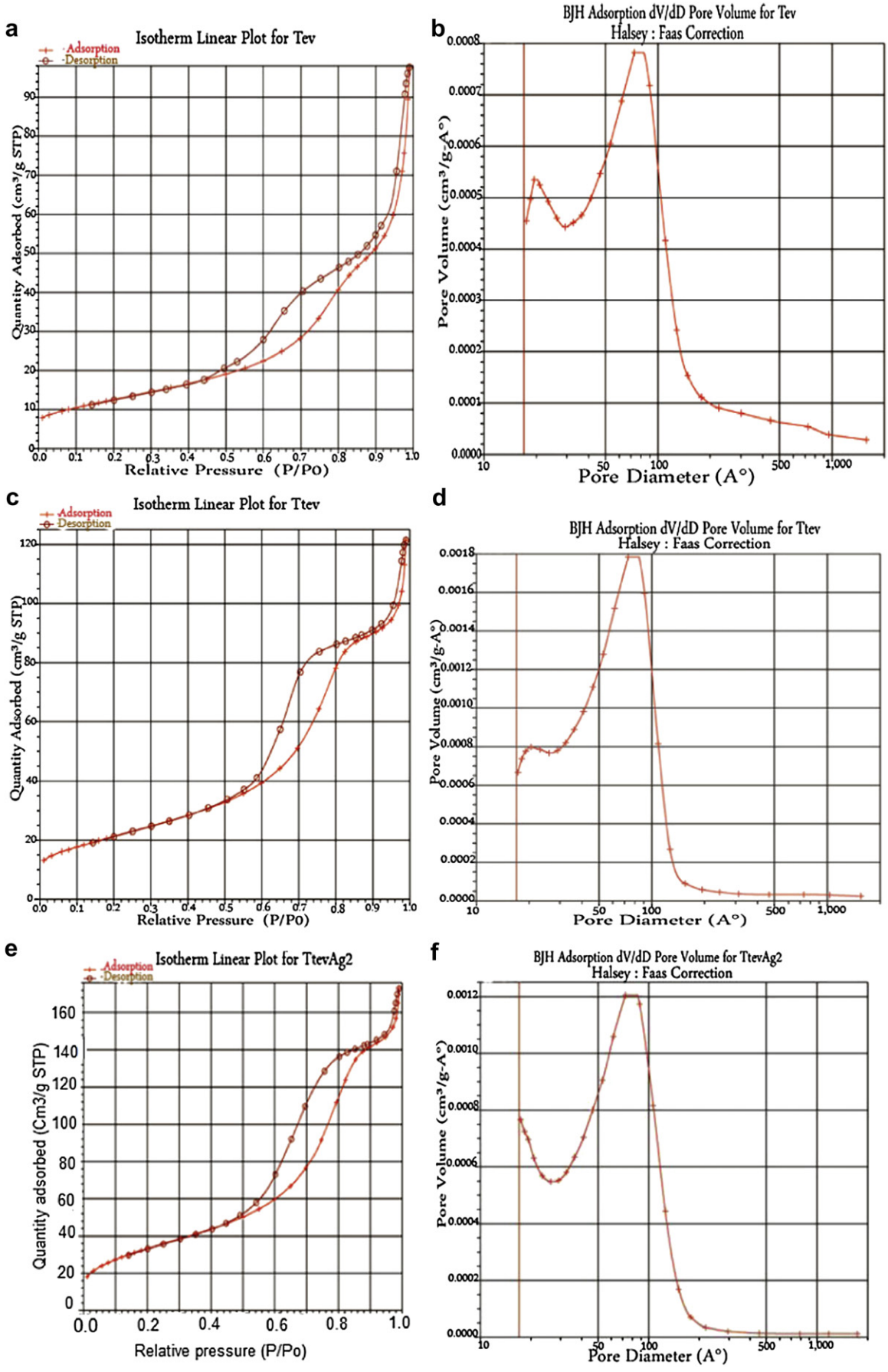

Fig. 3. (a,b) Isotherm plot and BJH adsorption d*v*/d*D* pore volume of Tev. (c,d) Isotherm plot and BJH adsorption d*v*/d*D* pore volume of Ttev. (e,f) Isotherm plot and BJH adsorption d*v*/d*D* pore volume of $TtevAg_2$.

nanoporous with quite narrow pore-size distribution centered at 21 Å, as well as mesoporous distribution centered at 83 Å. The surface area decreased appreciably with incorporating Ag ions, as shown in Table 2 for $TevAg_2$, probably related to pore blockage by silver nanoparticles. The pore radius of $TevAg_2$ (14.7 nm) exceeds that of Tev (11.4 nm) probably due to enforcing the Ag nanoparticles to reside inside the pores and as a result a comparable decrease in the pore volume specifically mesoporous ones (Table 2) was perceived.

This reflects the high dispersion of Ag nanoparticles in the mesoporous network of $TevAg_2$, as depicted from TEM observation. More interestingly, The BJH pore diameter of the former sample did not show any change following Ag incorporation, pointing out that at such loading of Ag a nonvariance of the wall surfaces is perceived. According to the IUPAC classification, the Ttev sample (Fig. 3c) exhibited type IV isotherm, showing the characteristics of mesoporous structures with a two-step desorption pointing to the presence of a tailorable amount of both open and narrowed mesopores. The first desorption step in the margin of P/P^o 0.5–0.85 is assigned to the desorption of nitrogen from the open mesopores characterizing ink-bottle type of pores ($P/P^o > 0.5$). The second desorption step in the margin of P/P^o 0.85–1.0 is attributed to narrowing parts of the mesoporous channels and creating ink-bottle like sections in addition to slit-shaped type of pores [49–51]. The shape of the nitrogen adsorption–desorption isotherms is strongly influenced by the titania source; as shown in Fig. 3a and c, in the sense that Ttev exhibits only mesopores where Tev reveals a combination of both meso- and macropores. In addition, Ttev presented higher surface area and pore volume values than those depicted for Tev due to the enhancement of mesoporosity of the former comparatively. The PSD of Ttev (Fig. 3d) shows a bimodal distribution in the 19–25 Å range with a maximum at ≈22 Å (broad) and at ≈85 Å (broad) almost similar to the PSD derived for Tev (Fig. 3a) except that the narrow distribution band of the later was sharper. Fig. 3e of $TtevAg_2$ sample presented adsorption–desorption isotherm similar to that of Ttev except that the second desorption step in the high P/P^o range was more narrowed in the former due to Ag incorporation, informing the deposition of Ag in this particular part.

Decrement of surface area following Ag incorporation for $TtevAg_2$ could be associated with the disappearance of the nanoparticle structures in the lower limit of mesopores. This was confirmed from the pore size distributions (PSD) obtained in the microporosity range (Fig. 3f, left side) via the Barrett–Joyner–Halenda (BJH) model. From this Figure, the $TtevAg_2$ PSD shows a monomodal distribution in the 73–89 Å range with a maximum at ≈85 Å (broad) together with vanishing the distribution in the range 19–25 Å, shown in Ttev, revolving that Ag took over this type of pores. Thus, the clear decrease in BET surface area of $TtevAg_2$ (61.7 $m^2\ g^{-1}$) in comparison with the corresponding values of Ttev (77.53 $m^2\ g^{-1}$) is correlated not only to the disappearance of nanoparticles of titania present in the lower limit of mesopores due to deposition of Ag atoms but also due to blocking of some titania pores; specifically mesoporous ones, with Ag nanoparticles (see Table 2; V_{meso} for Ttev is 0.151 $cm^3\ g^{-1}$ vs. 0.115 $cm^3\ g^{-1}$ for $TtevAg_2$).

Table 2
Surface texturing properties of synthesized TiO_2 and Ag/TiO_2 derived from hybrid polymers template.

Sample name	S_{BET} ($m^2\ g^{-1}$)[a]	S_t ($m^2\ g^{-1}$)[b]	V_p ($cm^3\ g^{-1}$)[c]	r (nm)[d]	V_{micro} ($cm^3\ g^{-1}$)[e]	V_{meso} ($cm^3\ g^{-1}$)[f]
Tev	45.6	47.0	0.110	11.4	0.001	0.109
$TevAg_2$	25.9	26.2	0.075	14.7	0.004	0.074
Ttev	77.5	81.8	0.154	8.0	0.003	0.151
$TtevAg_2$	61.7	65.8	0.118	7.6	0.003	0.115
$TevAg_6$	29.9	31.0	0.082	12.9	0.001	0.081

[a] S_{BET}: BET surface area.
[b] S_t: t-Plot surface area derived from the t-plot.
[c] V_p: Pore volume.
[d] r: BJH adsorption average pore diameter.
[e] V_{micro}: t-Plot micropore volume.
[f] V_{meso}: Mesopore volume.

3.3. Optical absorption properties

Previous studies have illustrated that incorporation of metal ion into TiO_2 leads to a red shift of UV reflection [52,53]. From the UV–vis reflectance spectra of the samples seen in Fig. 4, the reflection range of TiO_2 samples synthesized using hybrid polymers either derived from isopropoxide (Tev) or butoxide (Ttev) shows a red shift for the UV–vis spectra compared with Ag incorporated TiO_2. The blue shift of Ag/TiO_2 composites is attributed to decreasing the titania particles size (quantized). The latter quantization; which was in agreement with the decrease of particles size of Ag containing samples, in the band structure of TiO_2, may improve the photoactivity since the electrons photoexcited that confined in the conduction band can elongate their life time. Thus, the electron hole recombination rate during the illumination of catalyst decreases [44–46]. Furthermore, the increase of the band gap energy can be attributed to the interface interaction due to the presence of Ag_2O oxides and/or Ag metal in the catalyst. This effect was also seen by Periyat et al. [54]. Obviously, the threshold of UV–Vis reflection spectrum of the sample Tev (420 nm) shifts to 405 nm in $TevAg_2$, signifying the presence of large amount of Ag nanoparticles. The broadness and intense absorption of the later spectrum ($TevAg_2$) in the 380–450 nm range with a maximum at ≈405 nm explains the effects of surface plasmon resonance (SPR) due to Ag nanoparticles. From the curve of Ttev a peak at 418 nm is observed emphasizing that changing the titanium source from isopropyl into n-butoxide did not affect the reflection edges and thus gives comparable E_g (∼2.95 eV) values. On the other hand, recognizing a peak at 415 nm for $TtevAg_2$ compared with 405 nm for $TevAg_2$ reflects the effect of titania precursor on the particle size; as determined by XRD. The peak red shift of the former sample compared to the later has to be ascribed to two factors [43,55] first the grow of the nanoparticles and second to the variance in the dielectric constant of titanium oxide matrix existed due to the varying ratios of amorphous/anatase phases as a result of

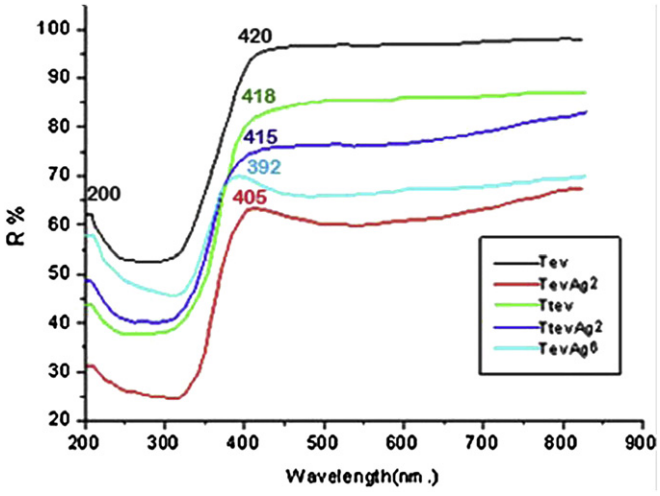

Fig. 4. Diffuse reflectance spectra of the catalysts Tev, $TevAg_2$, $TevAg_6$, Ttev, and $TtevAg_2$.

encapsulating Ag nanoparticles into titania structure, as elaborated from XRD results. The diffuse reflectance spectra demonstrated that compared to Tev, the reflection edge of the $TevAg_6$ sample was significantly blue-shifted to 393 nm compared to 420 nm; for Tev, which probably caused by quantum size and confinement effects.

3.4. FTIR spectra analysis

Poly(ethylene glycol-PEG1500) sample with molecular chemical structure ($HO–CH_2–(CH_2–O–CH_2)n–CH_2–OH$) used to have an important characteristic absorption band in the 1000–1300 cm^{-1} region associated with stretching vibration of ether groups i.e. C–O–C [56]. On the other hand, an absorption band at ν1142 cm^{-1} has been used as an assessment tool of polyvinyl alcohol (PVA) structure [57]. FTIR spectrum of the hybrid made of PVA/PEG shown in Fig. 5; to synthesize TiO_2 nanoparticles of Tev, reveals the absence of the mentioned two bands suggesting the interaction of the hybrid PEG/PVA together with the Ti precursor. The same was also seen for Ttev highlighting that changing the precursor of titanium from isopropyl to n-butoxide did not really affect the mode of interaction of PEG/PVA hybrid with the precursor source. In the case of the nanostructures derived from $TevAg_2$ and $TevAg_6$, bands at 1627, 1510, 1460, 1360 (1334), and 905 (830) cm^{-1} characterizing the conformation of OH (1627, 1510), deformation δ (CH_2, 1460, 1360 (1334) and CH_2 905 (830)) rocking were exhibited. The shift of OH deformation band (1627 cm^{-1}) into lower wavenumbers compared with those of Ag free TiO_2 samples (1633 cm^{-1}) is due to the chemical interaction between Ag and the hybrid PEG/PVA template. This gives strong evidence that the experimental procedure developed in this work was successful in obtaining and altering the organic–inorganic interaction between PVA/PEG and PVA/PEG/Ag. For the FTIR spectrum of $TtevAg_2$, other absorption bands positioned at 1580, 1245 and 1050 cm^{-1} were exposed and ascribed to the vibration of OH groups, and C–O stretching, respectively [58,59]. Simultaneously, the peak at 1633 cm^{-1} in Ttev is shifted to 1605 cm^{-1} in $TtevAg_2$ with a marked decrease in intensity indicating that the –OH groups in PVA had been partially decomposed after the reaction with Ag^+/Ag^o species and rather propose an interaction of Ag with O-atoms. In concordance, XRD lines of Ag_2O species were will clarified in this particular sample ($TtevAg_2$) and shapely present as well at 460 cm^{-1} suggesting the involvement of Ag–O bonds in the titania mesostructure.

3.5. Catalytic activity

The reduction of aromatic nitro compounds to amines is a very important process in synthetic organic chemistry and in industrial fabrication of many industrially important products. Aromatic nitro compounds are not reduced without a catalyst by metal boron hydrides (i.e. $NaBH_4$) in aqueous solution till 500 fold up increase in concentration of $NaBH_4$ relative to that of 4-NP. The reduction kinetics of nitro compounds was investigated accordingly as a decrease of the peak intensity at 400 nm for 4-NP. The catalytic activities of $P_{25}Ag_4$, Tev, Ttev, $TevAg_2$, $TtevAg_2$ and $TevAg_6$ were measured via the reduction of 4-NP as a model reaction and the results are shown in Fig. 6. The normalized temporal concentration changes (C/C_0) of 4-NP during the reduction were proportion to the normalized maximum absorbance (A/A_0) that derived from the changes in the 4-NP absorption profile (at 400 nm) at a given time interval. It was clear from Fig. 6 that the $TevAg_2$, $TtevAg_2$ and $TevAg_6$ catalysts showed significant progress in the reduction of 4-NP compared to $P_{25}Ag_4$, and they also exhibited higher efficiencies than Tev and Ttev those showed no activity at all under the same reaction condition confirming that Ag moieties are the active sites of the reaction. The 4-NPs were reduced by $TevAg_2$, $TtevAg_2$ and $TevAg_6$ in a time less than 4 min. In particular $TtevAg_2$ and $TevAg_6$ achieved 100% conversion within 2 min whereas $TevAg_2$ retained 97% conversion within 3 min. After adding $NaBH_4$ into the aqueous solution of 4-NP, the color of the solution changed from light yellow to dark yellow due to the formation of 4-nitrophenolate ion. Then, the color of the 4-nitrophenolate ions faded with time after the addition of $TevAg_2$, $TtevAg_2$ and $TevAg_6$ catalysts. The progress of the reaction that monitored by UV–vis spectroscopy shows a decrease for the characteristic peak of 4-NP at 400 nm, while at 300 nm a new peak began to appear due to 4-AP (Fig. 7). The reaction was finished within 200 s at 298 K. The reaction did not proceed in this period in the absence of Ag containing catalysts including $P_{25}Ag_4$ that did not show any activity. Fig. 8 shows a linear correlation between ln C_o/C and the reaction time at 298 K, indicating that the reaction is a pseudo-first-order. The k values for the conversion of 4-NP at 25 °C were 5.8×10^{-3}, 7.02×10^{-3} and 6.9×10^{-3} s^{-1} for $TevAg_2$, $TtevAg_2$ and $TevAg_6$, respectively. This kinetic results can be described by Langmuir–Hinshelwood model [60]; with the rate being proportional to the coverage θ, due to the

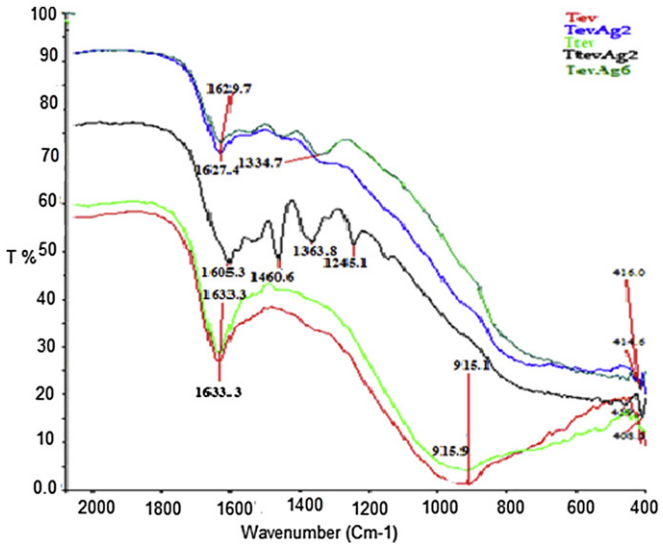

Fig. 5. FTIR spectra of Tev, $TevAg_2$, Ttev, $TtevAg_2$ and $TevAg_6$ samples.

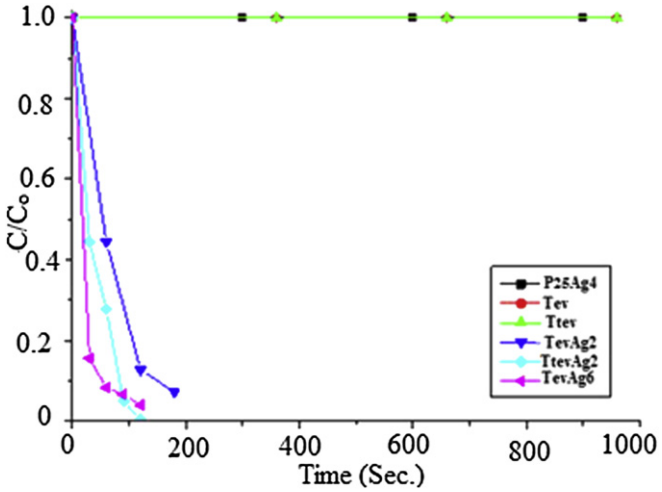

Fig. 6. The change in the concentration of 4-NP with time in the reduction of 4-NP by Tev, Ttev, $TevAg_2$, $TtevAg_2$, $TevAg_6$ and $P_{25}Ag_4$ catalysts in the presence of aqueous $NaBH_4$, reaction conditions: 100 ml [4-NP] = 1.8×10^{-4} mol L^{-1}, [$NaBH_4$] = 2.0×10^{-1} mol L^{-1}, 100 mg catalyst, 750 rpm, temperature 298 K.

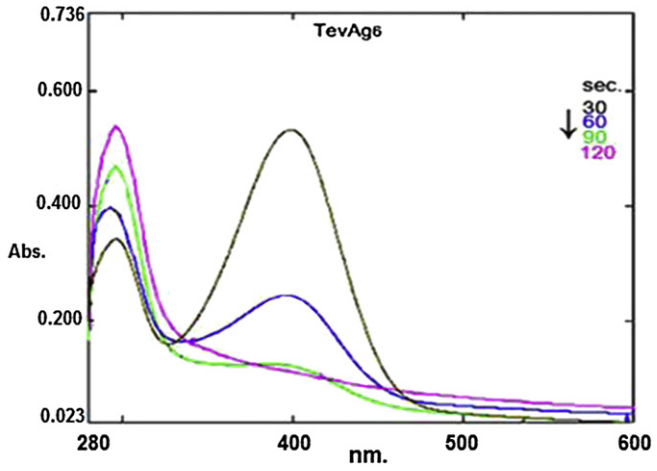

Fig. 7. UV–vis absorption spectra for the reduction of 4-NP over $TevAg_6$ with an excess amount of $NaBH_4$ in aqueous media at 298 K.

proposed reaction between adsorbate molecules (BH_4^- and 4NP) nevertheless no induction period is attained for this reaction reflecting the fast desorption of the product (only 2 min). $r = -dC/dt = k\theta = k\,KC/1 + KC$ (1), where k is the true rate constant which is dependent upon several parameters for example the catalyst mass, the flux of effective photons, etc., K the adsorption constant, t the time, and C is the concentration of organic pollutant (4-NP). For the low initial concentrations of pollutants, the term KC in the denominator can be ignored with respect to unity and the photocatalytic oxidation rate approaches first order: $r = -dC/dt = kKC = k\square\ C$ (2), where $k\square$ is the apparent rate constant of the pseudo-first order kinetics. The integral form, $C = f(t)$ of the rate equation is: $\ln C/C_0 = -k\square\ t$ (3); where C_0 is the initial concentration of 4-NP.

The stability and reusability of catalysts are very important issues for practical applications. The $TevAg_6$ and $TtevAg_2$ catalysts were reused in two successive reaction experiments (not shown) by simple filtration after reaction. The results obtained remains higher than 92% conversion in each cycle, confirming that $TevAg_6$ and $TtevAg_2$ catalysts are not corroded and rather stable during the catalytic reduction of 4-NP. Contrarily, the $TevAg_2$ catalyst showed deactivation (20% conversion) upon repeating the reaction once again without any treatment made for the catalyst following the first run except filtration.

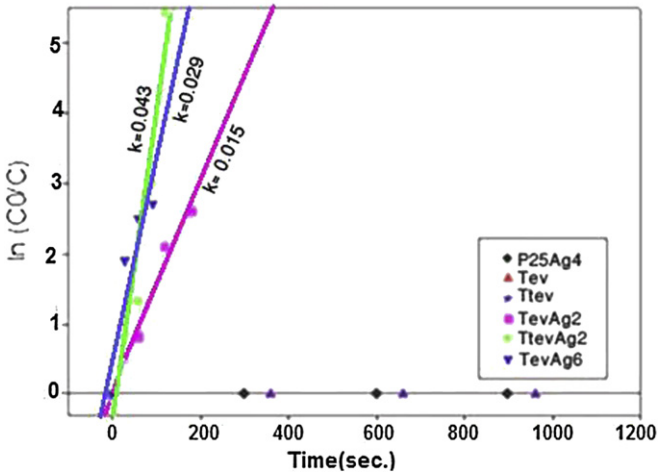

Fig. 8. ln C_o/C vs. time of Tev, Ttev, $TevAg_2$, $TtevAg_2$, $TevAg_6$ and $P25Ag_4$ catalysts.

The comparable high stability and rate constants of 4-nitrophenol reduction on $TtevAg_2$ and $TevAg_6$ exceeding that of $TevAg_2$ can be explained in view of the large surface area of the $TtevAg_2$ (61 $m^2\ g^{-1}$) catalyst. However, the relative decrease in surface area of $TevAg_6$, which showed comparable high activity as $TtevAg_2$, implies that surface area is not the only determining factor for the catalytic reduction of 4-NP. The catalytic difference between $TtevAg_2$ and $TevAg_6$ and that of $TevAg_2$ is attributed to other factors. Hence, we suggest that the well-ordered mesostructure of $TtevAg_2$ and $TevAg_6$; as depicted from surface texturing analysis, support the transport of the reactant 4-NP in the catalytic process and, thus, enhances the overall activity. This discloses that mesoporosity is a prerequisite for the high catalytic reduction activity of 4-NP. The second explanation for the higher catalytic activity and stability of the newly prepared mesoporous $TtevAg_2$ and $TevAg_6$ catalysts in comparison with $TevAg_2$ might be the size of the Ag nanoparticles. Although $TevAg_2$ presented the smallest Ag (2 nm) nanoparticles, it provided the lowest activity and stability comparatively whereas $TevAg_6$ that showed Ag nanopaticles of larger size comprised of 20 nm presented higher activity. It has been reported that smaller particles are more oxophilic thus exhibiting an increased BH_4^- adsorption. This might block the active sites for proper adsorption of the 4-NP followed by its reduction [61,62]. Thus, it is not necessarily that small particles as 2 nm exist active as such compared with 20 nm of Ag in $TevAg_6$. The difference in activity found for $TtevAg_2$ and $TevAg_6$ compared to $TevAg_2$ suggests that the rate of hydrogen transfer from BH_4^- adsorbed on mesoporous TiO_2 nanocrystals to adsorbed 4-NP is increased when Ag is incorporated into mesoporous TiO_2 networks i.e. facilitating hydrogen transfer to the pore surface.

Esumi et al. [63] have proposed that the catalytic reduction of 4-NP with $NaBH_4$ proceeded in two steps: (1) diffusion and adsorption of 4-NP to the Ag surfaces and (2) electron transfer mediated by Ag surfaces from BH_4^- to 4-NP. They have realized that the first step determined the reaction rate of 4-NP reduction. In this study, $TevAg_6$ and $TtevAg_2$ exhibited higher 4-NP reduction performance as well as stability than $TevAg_2$, suggesting that the AgNPs synthesized by our simple one pot method immobilized on TiO_2 have higher catalytic efficiencies than Ag catalysts prepared by the conventional co-precipitation method [64,65]. In the case of $TevAg_6$ and $TtevAg_2$ catalysts, Ag components are considered to exist not only on TiO_2 surfaces but also inside TiO_2 crystals. Specifically, in the case of $TevAg_6$ and $TtevAg_2$, most of AgNPs were well scattered on the entire surfaces of TiO_2 supports in the form of Ag_2O/Ag^o species rather than highly dispersed Ag^o nanoparticles as in $TevAg_2$ catalyst. Thus, such a unique surface distribution of Ag moieties could possibly contribute to efficient accessibility of the reactants to the catalytic active sites, resulting in excellent catalytic performances for $TevAg_6$ and $TtevAg_2$. When the reactions were conducted without stirring the $TevAg_6$ catalyst showed a much higher catalytic performance than the $TevAg_2$ catalyst, indicating the effective transport of the 4-NP to the Ag surfaces, even under static conditions. From these results, it can be suggested that the combination of a unique mesostructure, with an open porous nature, and the opportunity for $Ag_2O/AgNPs$ to be exposed to the reactants, contribute to the efficient transport of the 4-NP to the Ag surfaces, leading to an excellent catalytic activity for $TevAg_6$ and $TtevAg_2$ catalysts. Changes of morphology from spherical structure in $TevAg_2$ into bud ones with residual circular shape in $TevAg_6$ might also affect on the activity toward 4-NP reduction. However, in this specific case a direct correlation between the activity and shape of the catalyst cannot be fully achieved although the presence of the bud shape affects the activity when it presents in a proportion to the circular ones.

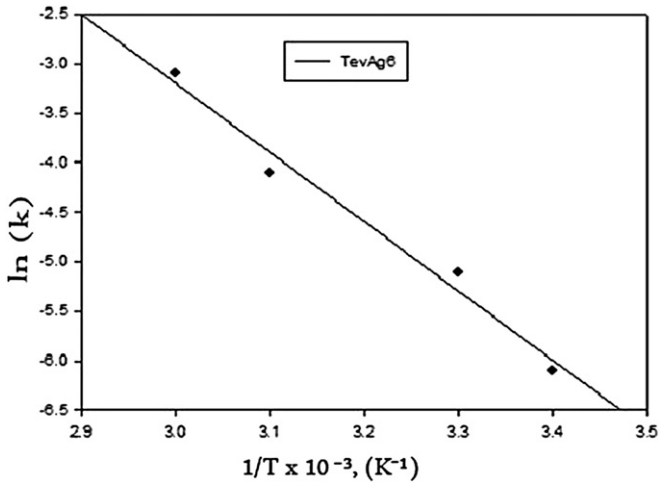

Fig. 9. Arrhenius plots of the rate constant of the reduction of 4-nitrophenol over the $TevAg_6$ catalyst.

Additionally, the activation energy parameter at different temperatures for 4-NP reduction on $TevAg_6$ was calculated from ln $k - 1/T$ (Fig. 9) equation. The activation energy for the reduction of 4-NP was 39.69 kJ mol^{-1}. The obtained activation energy was lower than other catalysts used to activate the same reaction such as Au/MAP (47 kJ mol^{-1}), silver nanoshell-coated cationic polystyrene beads (51 kJ mol^{-1}) and Au/polyelectrolyte brushes (43 kJ mol^{-1}) [62,63]. Normally, a reaction that is controlled by external mass transport (either gas–liquid or liquid–solid mass transport) has an activation energy of less than 25 kJ mol^{-1} [66,67]. Therefore, these high values of observed activation energies suggest that the influence of liquid–solid mass transport was negligible in this study. It appears also that the presence of appreciable amount of rutile percentages comprised of 24% in $TtevAg_2$ could also do share in increasing the activity comparatively. This is because of the possibility of forming many hetero-junctions such as anatase/rutile, Ag/anatase and Ag/rutile on which electrons can move to improve the activity toward the reduction process [68,69]. In addition, the presence of residual C–O species on the $TtevAg_2$ catalyst as a result of the non-complete decomposition of the template can do share in the oxidation of Ag^o into Ag^+ with subsequent reduction of Ag^+ by BH_4^- considering that the in situ reduction of Ag^+ is very important to this reduction reaction.

4. Conclusion

We demonstrated a facile hydrothermal one pot method for synthesizing Ag/TiO_2 nanoparticles via employing either isopropoxide or tetrabutyl as a titanium precursor and polyvinyl alcohol and polyethylene glycol as hybrid template. A marked higher reduction rate of 4-NP to 4-AP was achieved on $TevAg_6$ and $Ttevag_2$ catalysts in 2 min reaction time with 100% conversion and they rather show significant stability upon reusability. This excellent performance of the mentioned catalysts was attributed to the following aspects: (1) the presence of exposed Ag_2O species beside dispersed Ag nanoparticles on the surface of TiO_2 nano-buds (nano-circular) result in a higher catalytic reduction of 4-NP; (2) the mesoporous architecture and surface texturing properties specifically S_{BET} and pore volume contributes well to increasing the activity through facilitating both adsorption and diffusion processes; (3) Ag nanoparticles of medium sizes comprised of 15–20 nm facilitate the adsorption of BH_4^- besides phenolate ions rather than smaller ones (2 nm) leading to an enhanced catalytic activity.

Acknowledgments

Authors are indebted to King Abdul Aziz City for Science and Technology (KAST-Saudi Arabia) for funding the work number (94-17-اط) from which this text is produced.

References

[1] A. Saha, B. Ranu, J. Org. Chem. 73 (2008) 6867.
[2] A. Rahman, S.B. Jonnalagadda, Catal. Lett. 123 (2008) 264.
[3] F. Cardenas-Lizana, S. Gomez-Quero, M.A. Keane, Catal. Commun. 9 (2008) 475.
[4] A. Vass, J. Dudas, J. Toth, R.S. Varma, Tetrahedron Lett. 42 (2001) 5347.
[5] S.G. Harsy, Tetrahedron 46 (1990) 7403.
[6] Y. Zheng, K. Ma, H. Wang, X. Sun, J. Jiang, C. Wang, R. Li, J. Ma, Catal. Lett. 124 (2008) 268.
[7] V. Vishwanathan, V. Jayasri, P.M. Basha, N. Mahata, L.M. Sikhwivhilu, N.J. Coville, Catal. Commun. 9 (2008) 453.
[8] X.D. Wang, M.H. Liang, J.L. Zhang, Y. Wang, Curr. Org. Chem. 11 (2007) 299.
[9] B. Coq, F. Figueras, Coord. Chem. Rev. 178–180 (1998) 1753.
[10] K.R. Westerterp, E.J. Molga, K.B. van Gelder, Chem. Eng. Process. 36 (1997) 17.
[11] H. Lu, H. Yin, Y. Liu, T. Jiang, L. Yu, Catal. Commun. 10 (2008) 313.
[12] K.S. Shin, J.Y. Choi, C.S. Park, H.J. Jang, K. Kim, Catal. Lett. 133 (2009) 1.
[13] N. Yao, J. Chen, J. Zhang, J. Zhang, Catal. Commun. 9 (2008) 1510.
[14] G. Zhang, L. Wang, K. Shen, D. Zhao, H.S. Freeman, Chem. Eng. J 141 (2008) 368.
[15] K. Zhang, Y. Luo, Z. Li, Soft Mater. 5 (2007) 183.
[16] A. Corma, P. Serna, Science 313 (2006) 332.
[17] N.S. Chaubal, M.R. Sawant, J. Mol. Catal. A: Chem. 261 (2007) 232.
[18] Y. Mei, Y. Lu, F. Polzer, M. Ballauff, Chem. Mater. 19 (2007) 1062.
[19] Y. Lu, Y. Mei, R. Walker, M. Ballauff, M. Drechsler, Polymer 47 (2006) 4985.
[20] Y. Wang, G. Wei, F. Wen, X. Zhang, W. Zhang, L. Shi, J. Mol. Catal. A: Chem. 280 (2008) 1.
[21] L. Liu, B. Qiao, Y. Ma, J. Zhang, Y. Deng, Dalton Trans. 19 (2008) 2542.
[22] Y. Chen, C. Wang, H. Liu, J. Qiu, X. Bao, J. Chem. Soc. Chem. Commun. 42 (2005) 5298.
[23] J. Ning, J. Xu, J. Liu, H. Miao, H. Ma, C. Chen, X. Li, L. Zhou, W. Yu, Catal. Commun. 8 (2007) 1763.
[24] G.C. Bond, A.F. Rawle, J. Mol. Catal. A: Chem. 109 (1996) 261.
[25] F. Cardenas-Lizana, S. Gomez-Quero, M.A. Keane, ChemSusChem 1 (2008) 215.
[26] S. Jana, S.K. Ghosh, S. Nath, S. Pande, S. Praharaj, S. Panigrahi, S. Basu, T. Endo, T. Pal, Appl. Catal. A: Gen. 313 (2006) 41.
[27] F. Cardenas-Lizana, S. Gomez-Quero, N. Perret, M.A. Keane, Gold Bull. 42 (2009) 124.
[28] F. Cardenas-Lizana, S. Gomez-Quero, A. Hugon, L. Delannoy, C. Louis, M.A. Keane, J. Catal. 262 (2009) 235.
[29] D.S. Sidhaye, T. Bala, S. Srinath, H. Srinath, P. Poddar, M. Sastry, B.L.V. Prasad, J. Phys. Chem. C 113 (2009) 3426.
[30] B. Hammer, J.K. Norskov, Nature 376 (1995) 238.
[31] E. Bus, J.T. Miller, J.A. van Bokhoven, J. Phys. Chem. B 109 (2005) 14581.
[32] V. Iliev, D. Tomova, L. Bilyarska, A. Eliyas, L. Petrov, Appl. Catal. B 63 (2006) 266.
[33] Y. Zheng, C. Chen, Y. Zhan, X. Lin, Q. Zheng, K. Wei, J. Zhu, J. Phys. Chem. C 112 (2008) 10773.
[34] H.M. Sung-Suh, J.R. Choi, H.J. Hah, S.M. Koo, Y.C. Bae, J. Photochem. Photobiol. A: Chem. 163 (2004) 37.
[35] J. Selva, S.E. Martinez, D. Buceta, M.J. Rodriguez-Vazquez, M.C. Blanco, M.A. Lopez-Quintela, G. Egea, J. Am. Chem. Soc. 132 (2010) 6947.
[36] J. Liu, S.Z. Qiao, S.B. Hartono, G.Q. Lu, Angew. Chem. Int. Ed. 49 (2010) 4981.
[37] T. Murakata, Y. Higashi, N. Yasui, T. Higuchi, S. Sato, J. Chem. Eng. Jpn. 35 (2002) 1270.
[38] T. Sreethawong, Y. Suzuki, S. Yoshikawa, C. R. Chim. 9 (2006) 307.
[39] I. Paramasivalm, J.M. Macak, P. Schmuki, Electrochem. Commun. 10 (2008) 71.
[40] J. Joo, S.G. Kwon, T. Yu, M. Cho, J. Lee, J. Yoon, T. Hyeon, J. Phys. Chem. B 109 (2005) 15297.
[41] M.S. Sadjadi, N. Farhadyar, K. Zare, Superlattice Microstruct. 46 (2009) 483.
[42] G.P. Dong, X.D. Xiao, X.F. Liu, B. Qian, Z.J. Ma, S. Ye, D.P. Chen, J.R. Qiu, J. Nanopart. Res. 12 (2010) 1319.
[43] C.C. Li, K.L. Shuford, Q.H. Park, W.P. Cai, Y. Li, E.J. Lee, S.O. Cho, Angew. Chem. Int. Ed. 46 (2007) 3264.
[44] M. Zhou, S.H. Chen, S.Y. Zhao, H.F. Ma, Chem. Lett. 34 (2005) 1670.
[45] Y.G. Sun, Y.D. Yin, B.T. Mayers, T. Herricks, Y.N. Xia, Chem. Mater. 14 (2002) 4736.
[46] A. Gautam, G.P. Singh, S. Ram, Synth. Met. 157 (2007) 5.
[47] M.M. Mohamed, Appl. Catal. A: Gen. 267 (2004) 135–142. M.M. Mohamed, K.S. Khairou, Microporous Mesoporous Mater. 142 (2011) 130.
[48] C. He, Y. Xiong, J. Chen, C.H. Zha, X.H. Zhu, J. Photochem. Photobiol. A: Chem. 157 (2003) 71.
[49] P. Du, J.A. Moulijn, G. Mul, J. Catal. 238 (2006) 342.
[50] G. Mul, A. Zwijnenburg, B. van der Linden, M. Makkee, J.A. Moulijn, J. Catal. 201 (2001) 128.
[51] J.H. Pan, H. Dou, Z. Xiong, C. Xu, J. Ma, X.S. Zhao, J. Mater. Chem. 20 (22) (2010) 4461.

[52] C. Yu, H. Chu, Y. Wan, D. Zhao, J. Mater. Chem. 20 (2010) 4705.
[53] Y. Wang, Z.H. Jiang, F.J. Yang, Mater. Sci. Eng. B 134 (2006) 76.
[54] P. Periyat, K.V. Baiju, P. Mukundan, P.K. Pillai, K.G.K. Warrier, Appl. Catal. A: Gen. 349 (2008) 13.
[55] Y.H. Zhang, A. Reller, J. Mater. Chem. 11 (2001) 2537.
[56] A. Linsebigler, C. Rusu, J.T. Yates, J. Am. Chem. Soc. 118 (1996) 5284.
[57] W.-C. Yen, Y.-H. Lee, J.-F. Lin, C.-A. Dai, U.-S. Jeng, W.-F. Su, Langmuir 27 (1) (2011) 109.
[58] A. Henglein, Chem. Rev. 89 (1989) 1861.
[59] W.Y. Li, S. Seal, E. Megan, J. Ramsdell, K. Scammon, G. Lelong, L. Lachal, K.A. Richardson, J. Appl. Phys. 93 (2003) 9553.
[60] G. Al-Sayyed, J.C. D'Oliveira, P. Pichat, J. Photochem. Photobiol. A: Chem. 58 (1991) 99.
[61] D.C. Caskey, D.W. Chapman, US Patent 4 571 437 (1986), to Mallinckrodt Inc.
[62] T. Ishida, K. Kuroda, N. Kinoshita, W. Minagawa, M. Haruta, J. Colloid Interface Sci. 323 (2008) 105.
[63] K. Esumi, R. Isono, T. Yoshimura, Langmuir 20 (2004) 237.
[64] D.C. Caskey, D.W. Chapman, US Patent 4 415 753 (1983), to Mallinckrodt Inc.
[65] E.L. Derrenbacker, US Patent 4 307 249 (1981), to Mallinckrodt Inc.
[66] C.V. Rode, M.J. Vaidya, R.V. Chaudhari, US Patent 6 403 833 (2002), to Council of Scientific and Industrial Research.
[67] Z. Liu, X. Wang, H. Wu, C. Li, J. Colloid Interface Sci. 287 (2005) 604.
[68] X.Y. Liu, A.Q. Wang, X.F. Yang, T. Zhang, C.-Y. Mou, D.-S. Su, J. Li, Chem. Mater. 20 (2008) 4268.
[69] A. Ohnuma, E.C. Cho, P.H.C. Camargo, L. Au, B. Ohtani, Y. Xia, J. Am. Chem. Soc. 131 (4) (2009) 1352.